Title

Atomic-scale factors that control the rate capability of nanostructured amorphous Si for high-energy-density batteries

Authors

Artrith, Nongnuch
Urban, Alexander
Wang, Yan
et al.

Publication Date

2019-01-26

Peer reviewed

Atomic-scale factors that control the rate capability of nanostructured amorphous Si for high-energy-density batteries

Nongnuch Artrith* and Alexander Urban

Department of Materials Science and Engineering,

University of California, Berkeley, CA, USA

Yan Wang

Department of Materials Science and Engineering,

Massachusetts Institute of Technology, Cambridge, MA, USA

Gerbrand Ceder†

Department of Materials Science and Engineering,

University of California, Berkeley, CA, USA and

Materials Science Division, Lawrence Berkeley National Laboratory, Berkeley, CA, USA

(Dated: January 29, 2019)

Abstract

Nanostructured Si is the most promising high-capacity anode material to substantially increase the energy density of Li-ion batteries. Among the remaining challenges is its low rate capability as compared to conventional materials. To understand better what controls the diffusion of Li in the amorphous Li-Si alloy, we use a novel machine-learning potential trained on more than 40,000 *ab-initio* calculations and nanosecond-scale molecular dynamics simulations, to visualize for the first time the delithiation of entire LiSi nanoparticles. Our results show that the Si host is not static but undergoes a dynamic rearrangement from isolated atoms, to chains, and clusters, with the Li diffusion strongly governed by this Si rearrangement. We find that the Li diffusivity is highest when Si segregates into clusters, so that Li diffusion proceeds via hopping between the Si clusters. The average size of Si clusters and the concentration range over which Si clustering occurs can thus function as design criteria for the development of rate-improved anodes based on modified Si.

* nartrith@atomistic.net

† gceder@berkeley.edu

Lithium-ion batteries have enabled tremendous technological advances in consumer electronics and electric vehicles during the past decade [1], but to keep up with the growing demand for portable energy storage improved electrode materials with greater energy densities will be required. Over the last years, nanostructured Si has emerged as a promising high-capacity alternative to conventional graphite-based anodes [2–4]. However, while nanoscaling has allowed to overcome mechanical limitations such as fracturing [5], the rate-capability of silicon anodes is 2–4 orders of magnitude lower [6–8] than graphite's [9] owing to low Li mobility in the LiSi alloy, which considerably limits the power density. A detailed understanding of the nature of the relevant Li_xSi phases and the structural factors that control Li transport in the LiSi alloy is required for the rational design of Si-based anodes with improved Li mobility.

The lithiation of crystalline Si (c-Si) and the rich phase diagram of the LiSi alloy have been thoroughly investigated both by experiment [2, 10–16] and simulation [17–24]. Lithiation of c-Si at room temperature leads to the formation of an amorphous Li_xSi phase (a-Li_xSi) that crystallizes below ∼50 mV vs. Li^+/Li in the $Li_{15}Si_4$ structure [2, 11–13]. The a-Li_xSi and the c-$Li_{15}Si_4$ phases are metastable, but the crystalline ground states, c-Li_8Si_8 [25], c-$Li_{12}Si_7$ [26], c-Li_7Si_3 [27], c-$Li_{13}Si_4$ [28], and c-$Li_{21}Si_5$ [29], are only observed after annealing at higher temperatures [10]. After the first lithiation-delithiation cycle, lithium insertion and extraction only involves a-Li_xSi phases with intermediate compositions. Computational studies have been important to understand the mechanism of Li insertion into crystalline Si [21, 22, 24] and the resulting amorphization [17–19], to describe the topology of a-Li_xSi phases [23] and to relate the formation of Si−Si bonds to the mechanical properties of the material [30]. However, simulating Li transport through realistic amorphous LiSi structures requires large structure models limiting first-principles methods to molten LiSi phases at high temperatures and short time scales below 100 ps [20, 31], as the extensive sampling required to reach the time scales on which Li transport occurs at room temperature is not presently feasible. Additionally, the lack of long-range order prevents the use of experimental diffraction techniques for structure characterization, so that only indirect experimental information about the amorphous LiSi structures is available.

To shed light on the Li diffusion and extraction mechanism in nanostructured amorphous LiSi anodes, we employed advanced computational techniques to simulate the delithiation of entire LiSi nanoparticles on the atomic scale. Our simulations are based on a combination of

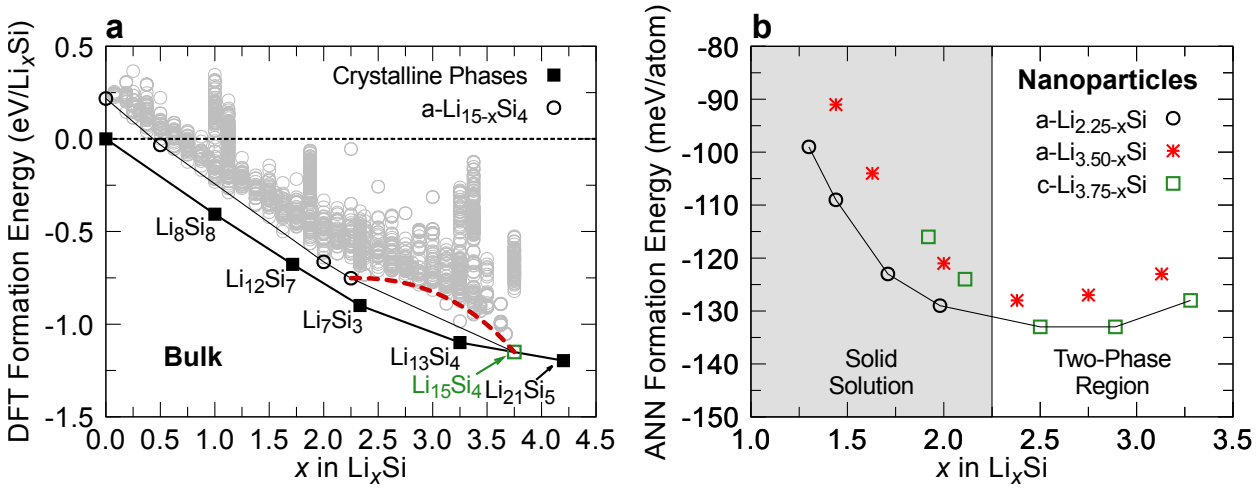

FIG. 1. **Crystalline $Li_{15}Si_4$ segregates from amorphous Li_xSi for $x > 2.25$.** **a**, Density-functional theory formation energies of the crystalline bulk Li_xSi_y structures (filled squares) and the amorphous bulk $Li_{15-x}Si_4$ structures samples for the present work (empty circles). The amorphous phase exhibits a two-phase region for $x > 2.25$ (red dashed line) in which phase separation into crystalline $Li_{15}Si_4$ (empty green square) and a-$Li_{2.25}Si$ is thermodynamically favored. **b**, The ANN potential formation energies of three nanoparticle models at different stages of delithiation after 4 ns equilibration at $T = 500\,\mathrm{K}$. Consistent with the bulk phase diagram in **a**, the most stable nanoparticle for compositions Li_xSi with $x > 2.25$ are derived from crystalline $Li_{15}Si_4$ (empty squares) whereas for $x < 2.25$ a solid solution behavior is observed (empty circles).

first-principles calculations and long-time-scale molecular dynamics (MD) simulations using highly accurate machine-learning potentials that have been carefully validated. The results elucidate how the clustering of Si atoms affects the Li diffusivity and identify structural motifs that are beneficial for Li transport, thereby providing a guideline for the design of Si-based anodes with improved rate capability.

I. ACCURATE NANOSCALE SIMULATIONS

To reach the length and time scales required for the simulation of Li transport through LiSi nanoparticles without sacrificing predictive accuracy, we developed a state-of-the-art artificial neural network (ANN) machine-learning potential [32–34] that was trained to reproduce density-functional theory (DFT) energies based on a reference set of 40,653 DFT bulk, cluster,

and surface structures with different compositions. Similar approaches have recently been successfully applied to the modeling of amorphous Si and LiSi alloy phases [35–38]. Our ANN potential achieves a root mean squared error of 7.7 meV/atom and a mean absolute error of 5.9 meV/atom relative to the DFT reference energies as determined based on an independent validation set of 4,516 randomly selected structures that were not used for training (**Fig. S1**). Supplementary **Fig. S2** and **Fig. S3** show that the formation energies of Li_xSi structures and the corresponding voltages predicted by the ANN potential are in excellent agreement with their DFT references. All DFT ground states are correctly reproduced by the ANN potential. Additionally, the ANN potential predicts Li diffusion barriers in excellent quantitative agreement with DFT, as we confirmed with transition path calculations using the *nudged elastic band* method [39, 40], and thus enables reliable molecular dynamics simulations (**Fig. S4** to **Fig. S6**). Further information about the parameters of the DFT calculations and the ANN potential can be found in the methods section.

II. AMORPHOUS Li_xSi BULK PHASE DIAGRAM

For the generation of amorphous Li_xSi bulk phases, a supercell of the c-$Li_{15}Si_4$ structure with composition $Li_{480}Si_{128}$ was computationally delithiated using a combination of the ANN potential and a genetic algorithm [35, 41]. The protocol used for the generation of bulk a-Li_xSi structures is detailed in the methods section, and a comparison with measured pair distribution functions from the literature confirms that the structures agree well with experiment (Supplementary **Fig. S7** and related discussion in the Supplementary Information). The formation energies of the resulting metastable amorphous structures, recomputed with DFT, are shown in **Fig. 1a** together with the ground-state hull defined by the crystalline LiSi phases. As seen in the figure, the amorphous phase diagram exhibits a two-phase region between $Li_{2.25}Si$ and $Li_{3.75}Si$ (= $Li_{15}Si_4$) in which phase separation into the end-members is favored. For compositions Li_xSi with $x < 2.25$ a solid-solution behavior is observed, i.e., each composition exhibits a formation energy on or close to the amorphous convex hull. A similar phase diagram has been previously reported based on simulations using a smaller cell size [42]. Bulk structure models are not appropriate to gain insight into the delithiation mechanism in actual LiSi nanostructures, but the bulk phase diagram provides a basis for the construction of reasonable nanoparticle models for subsequent investigation.

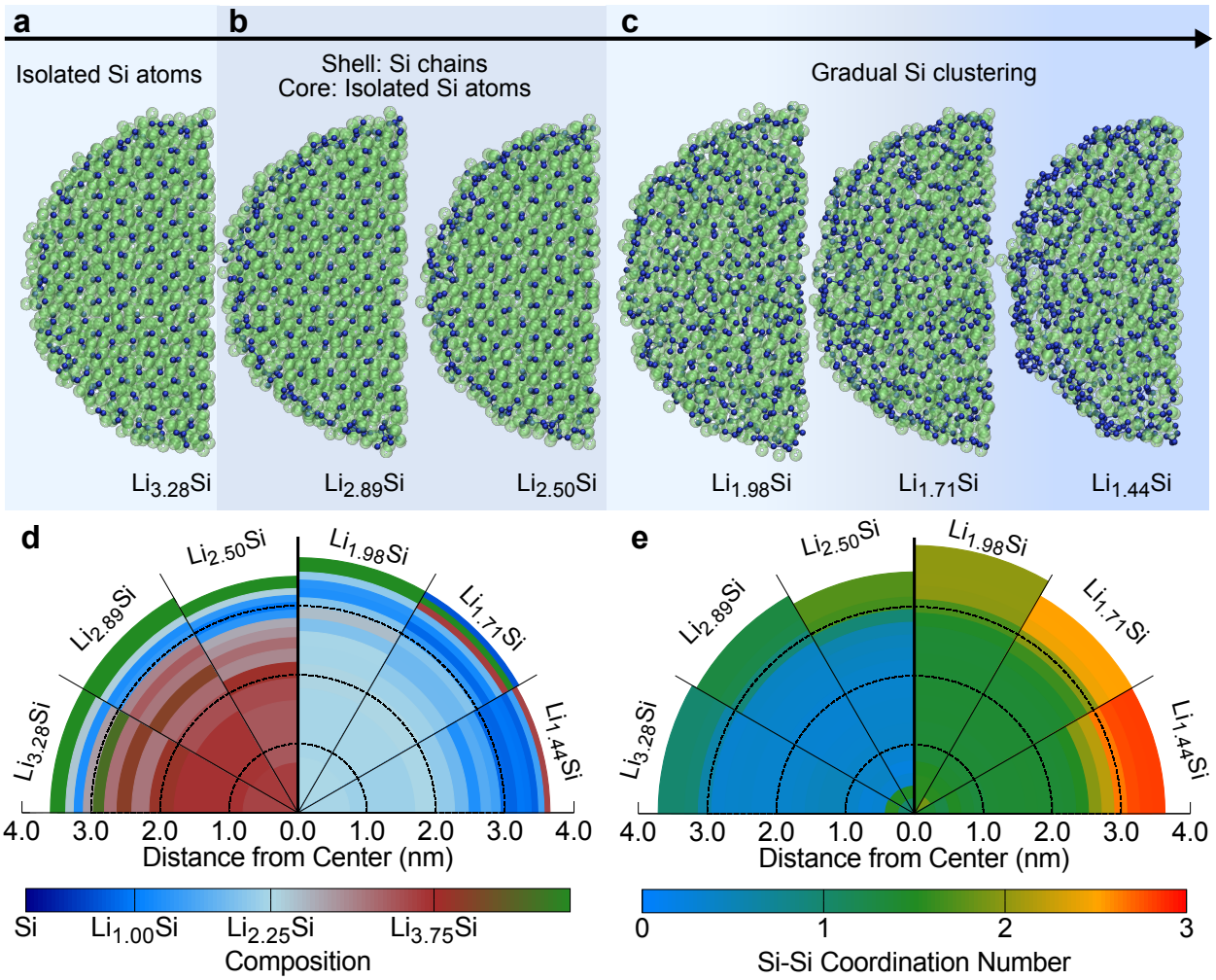

FIG. 2. **Si atoms segregate into clusters and chains during the delithiation of LiSi nanoparticles with 12,000 atoms. a–c**, Cross sections of nanoparticle structures corresponding to six stable phases of Fig. 1b with decreasing lithium content. The nanoparticles shown in **a** and **b** were obtained by delithiation of a c-$Li_{3.75}Si$ ($Li_{9429-x}Si_{2571}$) nanoparticle extracted from the $Li_{15}Si_4$ crystal structure. Li was sequentially removed from the particle surface followed by an equilibration with molecular dynamics simulations over 4 ns at 500 K at each composition. The structures in panel **c** were equivalently derived from a nanoparticle with original composition $Li_{2.25}Si$ ($Li_{8310-x}Si_{3690}$). Li and Si atoms are colored green and blue, respectively. **d**, Internal compositions of the nanoparticles as function of the distance from the particle center. The fully lithiated composition ($Li_{3.75}Si$) is colored red-brown, green regions are Li rich, and blue regions indicate relative delithiation. **e**, Si-Si coordination number as function of the distance from the particle center for the same nanoparticles. The data shown in **d** and **e** was obtained by averaging over the final 50 ps of 4 ns molecular dynamics trajectories at 500 K.

III. COMPUTATIONAL DELITHIATION OF LiSi NANOPARTICLES

To ensure the convergence of our simulations with particle size, we considered particles with different diameters between 2 and 8 nm and find that the structural motifs are converged for particle diameters between 6 to 8 nm (6,000–12,000 atoms). The following discussion is therefore based on the simulations of particles with diameters of around 8 nm corresponding to ∼12,000 atoms in their fully lithiated composition. *In situ* NMR measurements have previously revealed that the delithiation mechanism depends on the initial degree of lithiation [16]. This observation also agrees with the phase diagram in **Fig. 1a**. Therefore, we constructed nanoparticle structures by extraction from $Li_{15-x}Si_4$ bulk structure models with three different compositions, c-$Li_{3.75}Si$ (= $Li_{15}Si_4$), a-$Li_{3.50}Si$, i.e., within the bulk two-phase region, and a-$Li_{2.25}Si$, i.e., the fully lithiated end-member of the solid-solution phase.

At each delithiation step Li atoms were extracted from the particle surface, which was followed by a thermal equilibration over 4 ns at $T = 500$ K. To parallelize some of the computational effort, nanoparticle models of the next lower Li content were constructed based on the structure after 1 ns equilibration, as we generally found that sufficient Li atoms had migrated to the particle surface to allow for further delithiation. The potential energy during the MD simulations (**Fig. S8**) is generally converged after 2 ns showing that the structure of the nanoparticles has reached thermal equilibrium.

The formation energies of the various nanoparticle structures relative to elemental Li and Si are shown in **Fig. 1b**. For compositions Li_xSi with $x < 2.25$ the nanoparticle model based on the bulk a-$Li_{2.25}Si$ structure is most stable, for higher Li contents the delithiated crystalline $Li_{3.75-x}$ particles are lowest in energy. The nanoparticle structures based on the a-$Li_{3.50}Si$ is never stable, in accordance with the bulk phase diagram.

Figure 2a–c shows cross sections of six nanoparticle structures at different stages of delithiation that are on the ground-state hull in **Fig. 1b**. As seen in **Figure 2a–b**, Si chains and clusters first form in the outer regions of the particle upon delithiation, while the Si atoms in the core of the particle initially remain isolated. Continued Li extraction leads to the growth of the clustered phase from the particle surface towards the center. Once the overall composition $Li_{2.25}Si$ has been reached, the delithiation proceeds via a single-phase mechanism (**Figure 2c**), so that the length of the Si chains within the entire cluster increases upon Li extraction. Eventually, larger Si clusters form and as the overall composition reaches

$\sim Li_{1.3}Si$ the structure is dominated by Si clusters and chains.

Note that the predicted delithiation mechanism is fully consistent with previously reported experimental evidence [14–16]. However, our simulations allow for the first time to unambiguously characterize the atomic structures of all phases occurring during the delithiation. For this purpose, the internal composition and the nature of the Si clustering as function of the distance from the particle center at different stages of delithiation is shown in **Figure 2d–e**. This data was determined by computing histograms for the final 50 ps of the corresponding 4 ns MD trajectories using spherical bins with equal volume.

As seen in **Figure 2d**, during the initial stages of delithiation the core of the particle remains close to the original $Li_{3.75}Si$ composition. Further, the Li concentration does not decrease monotonously from the particle center towards the surface, but instead reaches a local minimum at a distance of around three fourth of the particle radius. This is the phase that grows during delithiation in the two-phase regime.

Once the Li content drops below 2.25, a more homogeneous delithiation is energetically favored, so that the Li content in nanoparticles with compositions $Li_{1.98}Si$, $Li_{1.71}Si$, and $Li_{1.44}Si$ decreases continuously from the particle center to the surface.

We stress that until an overall composition of $Li_{1.71}Si$ has been reached, Li is the predominant species at the particle surface after equilibration, indicating that the simulated delithiation rate is not too fast. For the particle with lower Li content ($Li_{1.44}Si$) the surface contains some Si, evidencing that the overall composition has not equilibrated on the time scale of our simulation. The Li content can therefore be expected to homogenize further on experimental time scales in the $Li_{1.71}Si$ and $Li_{1.44}Si$ compositions.

Note that the driving force for the Li atoms to migrate to the particle surface in our simulations is the lower Li surface energy as compared to Si. In an actual electrochemical cell the lower free energy of oxidation of Li can be expected to have a similar effect.

The Si clustering behavior can be further quantified by considering the Si−Si coordination number, shown for a bond-length cutoff of 2.7 Å in **Figure 2e**. As seen in the figure, Si atoms in the center of the particle remain mostly isolated as long as the composition in the particle core remains close to $Li_{3.75}Si$. The Si clustering in Li_xSi with $2.25 < x < 3.75$ is more pronounced near the surface as evidenced by the higher coordination numbers. Based on the coordination number, the Si clustering is similar to the one in the $Li_{2.25}Si$ phase with an average coordination 1.0–1.5, corresponding to Si dimers and trimer chains. Further

TABLE I. **Li diffusivity determined by molecular dynamics simulations.** Calculated activation energies E_a for Li diffusion in amorphous Li_xSi and Arrhenius-extrapolated diffusivity D at room temperature.

x_{Li}	E_a (eV)	D (cm^2s^{-1})
0.75	0.789 ± 0.022	$(1.154 \pm 1.084)\times10^{-14}$
1.00	0.500 ± 0.015	$(5.986 \pm 3.722)\times10^{-11}$
2.25	0.483 ± 0.010	$(9.607 \pm 3.805)\times10^{-11}$
3.50	0.682 ± 0.027	$(3.820 \pm 4.691)\times10^{-13}$

delithiation to $Li_{2.25-x}Si$ compositions results in a more homogeneous clustering behavior with continuously increasing coordination number from the particle center to the surface.

IV. Li DIFFUSIVITY IN THE RELEVANT LiSi PHASES

The nanoparticle simulations resolve the structure of the LiSi alloy at different states of charge and identify the particular importance of the $Li_{3.75}Si$ ($Li_{15}Si_4$) and $Li_{2.25}Si$ phases that exhibit fundamentally different Si clustering behavior. To understand how the Si clustering affects the Li diffusion mechanism and the Li diffusivity, we carried out 5 ns long MD simulations of bulk structures with the initial nanoparticle compositions ($Li_{3.75}Si$, $Li_{3.50}Si$, and $Li_{2.25}Si$) and with the composition of a further delithiated phase with increased Si clustering ($Li_{1.00}Si$). In light of the low measured Li diffusivities on the order of 10^{-10}–10^{-14} cm^2s^{-1} [6–8, 43–45] (see also Table S1), elevated temperatures (400 K, 500 K, 600 K, 700 K, 800 K, 900 K, 1000 K, 1100 K, and 1200 K) were chosen, so that sufficient Li hopping events occur on the timescale of the simulation. Room temperature diffusivities were obtained by Arrhenius extrapolation, which has proven reliable for similar applications [46]. Since the lowest melting temperature of any Li_xSi composition is 865 K for $Li_{0.75}Si$ [11], i.e., below the maximal temperatures in our simulations, we confirmed that for simulations above 800 K the time scale was too short for melting to occur, allowing us to capture diffusion in the solid state.

The computed room-temperature Li diffusivities and the corresponding activation energies shown in **Table I** vary strongly with the composition and span a large range. In the

fully lithiated $Li_{3.75}Si$ structure, the diffusivity is lowest and is indistinguishable from zero in our MD simulations. Delithiation to $Li_{3.50}Si$ results in an improved but still low Li diffusivity of $\sim 10^{-13}\,cm^2s^{-1}$. A significantly higher diffusivity of $>10^{-11}\,cm^2s^{-1}$ is found for the clustered amorphous $Li_{2.25}Si$ and $Li_{1.00}Si$ compositions. At lower Li contents Si forms extended networks throughout the structure impeding Li diffusion, and the Li diffusivity in the $Li_{0.75}Si$ composition is only $\sim 10^{-14}\,cm^2s^{-1}$. Note that the predicted diffusivities for all delithiated compositions fall into the experimentally measured range, though the variation of the diffusivity with the state of charge depends on the morphology and size of the electrode particles and the prevailing delithiation mechanism (single-phase or two-phase).

V. UNDERSTANDING Li DIFFUSION IN THE PRESENCE OF Si CLUSTERS

The drastic change of the Li diffusivity with the composition indicates a strong dependence of the Li transport on the distribution of Si atoms throughout the material. By visualizing the Li trajectories we observed that Li atoms spend much time in the vicinity of Si clusters and only occasionally hop between different clusters.

To better understand the extent to which the Li mobility in the different Li_xSi phases is determined by the presence of Si clusters, we analyzed 5 ns long trajectories with respect to the effect of coordinating Si atoms on the diffusion velocity of all Li atoms. For this analysis, we assigned to each Li atom all Si atoms within a cutoff range of 3.5 Å over the course of the MD simulation, which allows us to determine the average Li diffusion velocity as a function of the Si coordination number. The results for those coordination numbers that occur with a frequency of at least 1% are shown in **Fig. 3a** for the three compositions $Li_{3.75}Si$, $Li_{2.25}Si$, and $Li_{1.00}Si$.

The insights from the coordination analysis are **(i)** that the Li diffusion velocity decreases steeply with increasing Si coordination number, indicating a strong Li-Si interaction. **(ii)** The highest atomic velocity for Li atoms coordinated by 2 Si atoms is nearly identical for the three considered compositions. **(iii)** The differences in overall Li diffusivity instead arise from the different distribution of coordination numbers in the three compositions (**Fig. S9**): During the simulation of the crystalline $Li_{3.75}Si$ structure Li is symmetrically coordinated by exactly 3 Si atoms more than 80% of the time, locking the Li atom in place. Lower coordinations occur with only close to 1% probability. However, in the amorphous $Li_{2.25}Si$

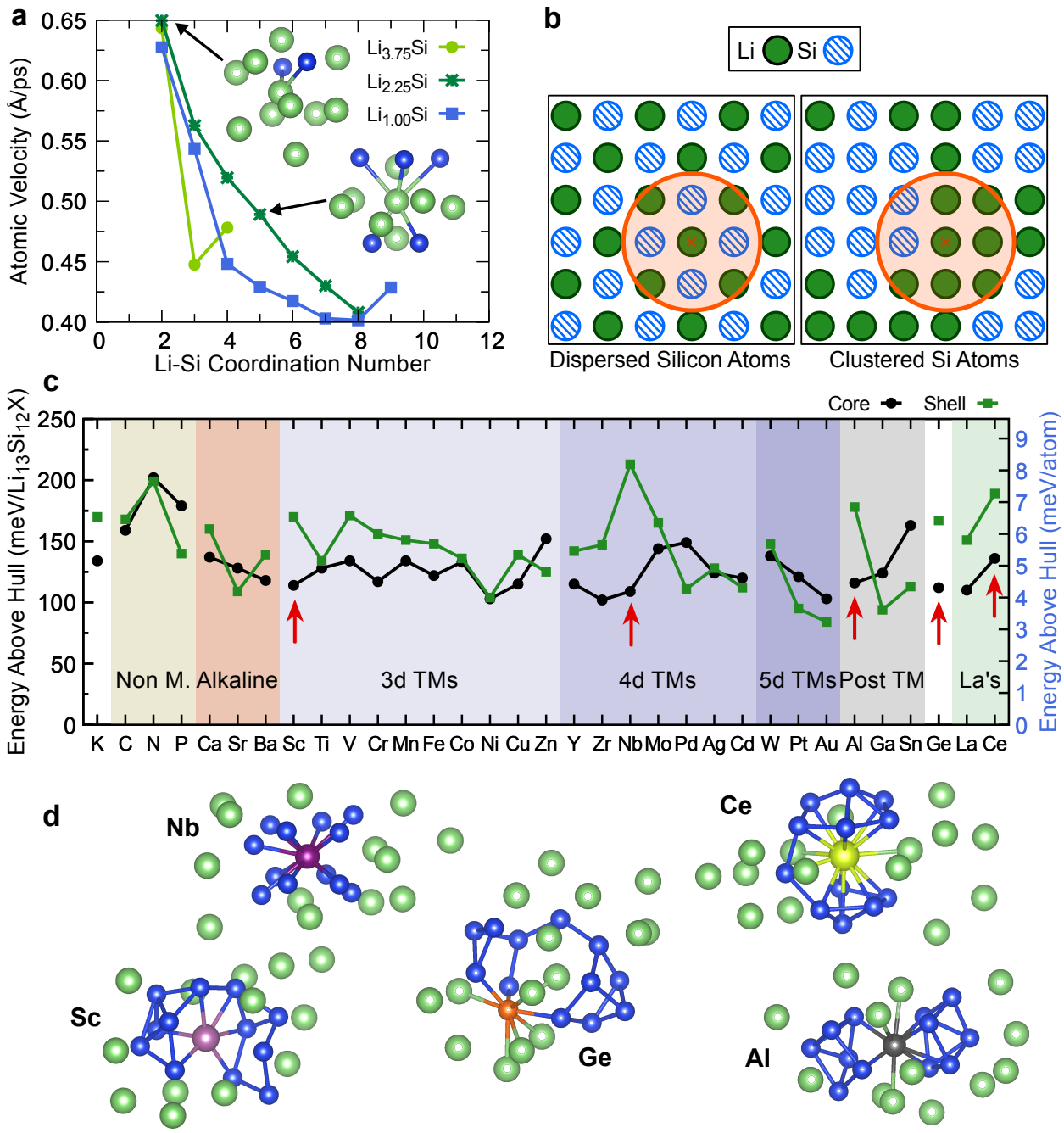

FIG. 3. **Si segregation is beneficial for Li diffusion.** **a**, The average velocity of Li atoms as function of the number of Si atoms within 3.5 Å around them. The velocity decreases with increasing number of Si atoms. Two representative Li environments with two and five Si atoms are shown in the insets. **b**, Schematic showing that the average Li-Si coordination number decreases when Li and Si segregate into separate domains. **c**, Decomposition energies of Si clusters embedded in Li doped with a third species X either on the surface (shell; green squares) or inside (core; black circles) of the Si cluster with composition $Li_{13}Si_{12}X$. The five systems for which the core structure is most stabilized are indicated with red arrows. **d**, Optimized geometries of the five core-doped $Li_{13}Si_{12}X$ compositions highlighted in panel **c**.

and $Li_{1.00}Si$ compositions the probability of a coordination number of 2 is increased relative to the $Li_{3.75}Si$ phase even though the average Si coordination number is greater because of the reduced Li content.

The *increased* amount of Li atoms with low Si coordination number at *decreased* Li content can be understood in the context of Si clustering. As schematically shown in **Fig. 3b**, Si segregation in form of clustering reduces the average number of Si atoms around Li. Since Li diffuses fast only when it detaches from a Si cluster or chain, the Li diffusion mechanism is akin to Li hopping between Si clusters. A maximal overall Li diffusivity would therefore be expected for a structure with perfect Si segregation into large clusters.

The diffusivity D in such a *discrete* lattice site hopping model can be expressed as [47, 48]

$$D = \rho\lambda^2\Gamma$$

where Γ is the hopping rate between Si clusters, and λ is the mean distance between the Si clusters, and the geometry factor ρ depends on the spatial arrangement of the clusters. Hence, the diffusivity increases approximately quadratically with the mean cluster distance λ. The hopping rate Γ can be taken to be constant as it is determined by the probability of Li atoms to be trapped near a Si cluster and thus mainly depends on the Li-Si interaction strength. Assuming that the density of the LiSi alloy is independent of the arrangement of the Si atoms, the mean free distance between Si clusters in a close-packed structure is proportional to the average cluster diameter. This important finding explains why Si clustering is beneficial for Li diffusion, as it increases the mean free distance between Si atoms compared to homogeneously dispersed isolated Si atoms. Si clustering can thus function as a design criterion for the engineering of improved Si-based anodes, for example, as composite materials [49, 50] or by co-alloying or doping of other chemical species. It is known from other alloys that even small dopant concentrations can promote the segregation of some of the constituents [51].

To demonstrate that doping can in fact improve the Si clustering in the LiSi alloy, we evaluated the DFT energy of doped model Si clusters. Using the Materials Project open database [52], we identified potential dopant species that are known to form compounds with Si but not with Li. Other common species in Si compounds such as C were also considered, giving a total of 33 dopant species.

To determine in a first approximation whether the dopants would favor Si clustering, an

initial structure of icosahedral 13-atom Si clusters surrounded by 13 Li atoms in a periodic close-packed arrangement was constructed. From this ideal cluster model, two structures were derived for each dopant species (**Fig. S10**): One structure in which the central Si atom of the Si_{13} cluster is replaced by the dopant atom (*core* model) and one structure in which one of the other 12 equivalent Si atoms is replaced (*shell* model). Both core and shell structures and the lattice parameters were optimized with DFT calculations, and the resulting formation energies are shown in **Fig. 3c**.

As seen in the figure, the core doping is favored by 21 out of 33 dopants, and the energy above the hull is generally below 10 meV/atom. The largest stabilization of the core-doped structure is observed for doping with Sc, Nb, Al, Ge, and Ce (red arrows in **Fig. 3c**). The optimized core-doped structures for those dopant species are shown in **Fig. 3d**, and the most well-defined clustering occurs for Nb and Ce. Note that the Materials Project database contains Si compounds with both Nb and Ce but does not contain any stable Li-Nb or Li-Ce compounds (**Fig. S11**). Doping with the 4d transition metal Mo [53] and with the Lanthanides La [54, 55] and Gd [56] has previously been reported to enhance the electrochemical properties of the LiSi alloy, further showing that an improvement by Nb and Ce doping is plausible.

While this simple computational screening should just be considered a proof of concept, it demonstrates that doping will indeed affect the Si clustering behavior. Further investigation will be required to determine whether the doped phases are stable at operation conditions and to understand the effect of doping on the Li-Si interaction strength.

Our results give important insight into the unusual delithiation and diffusion mechanism of Li in Si. The findings also point out several avenues towards improved Li transport in Si-based anodes. The Li diffusivity can be enhanced by favoring the formation of larger Si clusters over a wider range of Li_xSi compositions. Compositional additives that improve the Si mobility are more likely to lead to such larger clusters. Similarly, the Li diffusivity could be improved by increasing the effective rate by which Li hops between the Si clusters by co-alloying with other species which preferentially bind to the surface of the Si cluster and reduce the attraction between Li and these surfaces. Ideally, the Li-Si surface interaction would be equal to the Li-Li interaction causing Li to freely hop from cluster to cluster.

VI. CONCLUSIONS

Using newly developed neural network potentials we were able to simulate the complex diffusion of lithium in crystalline and amorphous silicon nanoparticles. We found as Li is extracted from a highly lithiated nanoparticle, Si segregates into clusters and chains affecting the Li transport. Li-rich domains lead to high Li mobility whereas an increasing coordination by Si slows down diffusion as Li mostly diffuses around Si clusters. Owing to this mechanism, the Li diffusivity in the clustered phase is with around $10^{-11}\,\mathrm{cm^2 s^{-1}}$ several orders of magnitude higher than the diffusivity in phases with isolated Si atoms. Increasing the cluster size or reducing the Li-Si surface interaction would all help in increasing the Li transport through silicon. This finding indicates that the low rate-capability of anodes based on amorphous Si is not inevitable but could in fact be avoided if the formation of Si clusters at higher lithium concentrations could be promoted.

VII. ACKNOWLEDGEMENTS

The authors thank China Automotive Battery Research Institute, Co., Ltd. and General Research Institute for NonFerrous Metals (GRINM) for financial support. This work used the computational facilities of the Extreme Science and Engineering Discovery Environment (XSEDE), which is supported by National Science Foundation Grant No. ACI-1053575. Additional computational resources from the University of California Berkeley, HPC Cluster (SAVIO) and from the Lawrencium computational cluster resource provided by the IT Division at the Lawrence Berkeley National Laboratory (Supported by the Director, Office of Science, Office of Basic Energy Sciences, of the U.S. Department of Energy under Contract No. DE-AC02-05CH11231) are also gratefully acknowledged.

VIII. AUTHOR CONTRIBUTIONS

G.C. and N.A. conceived the project. G.C. supervised all aspects of the research, contributed to the data analysis and to writing the manuscript. N.A. developed the ANN potential, carried out DFT calculations and MD simulations, analyzed the data, and authored the manuscript. A.U. provided the genetic algorithm and contributed to the data analysis and to writing the manuscript. Y.W. performed preliminary DFT calculations and contributed to the discussion.

[1] J. B. Goodenough and K.-S. Park, J. Am. Chem. Soc. **135**, 1167 (2013).

[2] M. T. McDowell, S. W. Lee, W. D. Nix, and Y. Cui, Adv. Mater. **25**, 4966 (2013).

[3] X. Su, Q. Wu, J. Li, X. Xiao, A. Lott, W. Lu, B. W. Sheldon, and J. Wu, Adv. Energy Mater. **4**, 1300882 (2013).

[4] M. R. Zamfir, H. T. Nguyen, E. Moyen, Y. H. Lee, and D. Pribat, J. Mater. Chem. A **1**, 9566 (2013).

[5] B. Wang, X. Li, B. Luo, L. Hao, M. Zhou, X. Zhang, Z. Fan, and L. Zhi, Adv. Mater. **27**, 1526 (2015).

[6] N. Ding, J. Xu, Y. Yao, G. Wegner, X. Fang, C. Chen, and I. Lieberwirth, Solid State Ionics **180**, 222 (2009).

[7] J. Xie, N. Imanishi, T. Zhang, A. Hirano, Y. Takeda, and O. Yamamoto, Mater. Chem. Phys. **120**, 421 (2010).

[8] J. Li, X. Xiao, F. Yang, M. W. Verbrugge, and Y.-T. Cheng, J. Phys. Chem. C **116**, 1472 (2012).

[9] M. Park, X. Zhang, M. Chung, G. B. Less, and A. M. Sastry, J. Power Sources **195**, 7904 (2010).

[10] C. J. Wen and R. A. Huggins, J. Solid State Chem. **37**, 271 (1981).

[11] P. Limthongkul, Y.-I. Jang, N. J. Dudney, and Y.-M. Chiang, Acta Mater. **51**, 1103 (2003).

[12] M. N. Obrovac and L. Christensen, Electrochem. Solid-State Lett. **7**, A93 (2004).

[13] J. Li and J. R. Dahn, J. Electrochem. Soc. **154**, A156 (2007).

[14] M. T. McDowell, S. W. Lee, J. T. Harris, B. A. Korgel, C. Wang, W. D. Nix, and Y. Cui, Nano Lett. **13**, 758 (2013).

[15] J. W. Wang, Y. He, F. Fan, X. H. Liu, S. Xia, Y. Liu, C. T. Harris, H. Li, J. Y. Huang, S. X. Mao, and T. Zhu, Nano Lett. **13**, 709 (2013).

[16] K. Ogata, E. Salager, C. Kerr, A. Fraser, C. Ducati, A. Morris, S. Hofmann, and C. Grey, Nat. Commun. **5**, 3217 (2014).

[17] V. L. Chevrier, J. W. Zwanziger, and J. R. Dahn, Can. J. Phys. **87**, 625 (2009).

[18] V. L. Chevrier and J. R. Dahn, J. Electrochem. Soc. **156**, A454 (2009).

[19] V. L. Chevrier and J. R. Dahn, J. Electrochem. Soc. **157**, A392 (2010).

[20] H. Kim, C.-Y. Chou, J. G. Ekerdt, and G. S. Hwang, J. Phys. Chem. C **115**, 2514 (2011).

[21] M. K. Y. Chan, C. Wolverton, and J. P. Greeley, J. Am. Chem. Soc. **134**, 14362 (2012).

[22] E. D. Cubuk, W. L. Wang, K. Zhao, J. J. Vlassak, Z. Suo, and E. Kaxiras, Nano Lett. **13**, 2011 (2013).

[23] E. D. Cubuk and E. Kaxiras, Nano Lett. **14**, 4065 (2014).

[24] H. Jung, M. Lee, B. C. Yeo, K.-R. Lee, and S. S. Han, J. Phys. Chem. C **119**, 3447 (2015).

[25] L. A. Stearns, J. Gryko, J. Diefenbacher, G. K. Ramachandran, and P. F. McMillan, J. Solid State Chem. **173**, 251 (2003).

[26] R. Nesper, H. G. von Schnering, and J. Curda, Chem. Ber. **119**, 3576 (1986).

[27] H.-G. V. Schnering, R. Nesper, J. Curda, and K.-F. Tebbe, Zeitschrift fur Metallkunde **71**, 357 (1980).

[28] U. Frank, W. Müller, and H. Schäfer, Z. Naturforsch. **30**, 10 (2014).

[29] R. Nesper and H. G. von Schnering, J. Solid State Chem. **70**, 48 (1987).

[30] K. Zhao, W. L. Wang, J. Gregoire, M. Pharr, Z. Suo, J. J. Vlassak, and E. Kaxiras, Nano Lett. **11**, 2962 (2011).

[31] C.-Y. Chou and G. S. Hwang, J. Power Sources **263**, 252 (2014).

[32] J. Behler and M. Parrinello, Phys. Rev. Lett. **98**, 146401 (2007).

[33] N. Artrith and A. Urban, Comput. Mater. Sci. **114**, 135 (2016).

[34] N. Artrith, A. Urban, and G. Ceder, Phys. Rev. B **96**, 014112 (2017).

[35] N. Artrith, A. Urban, and G. Ceder, J. Chem. Phys. **148**, 241711 (2018).

[36] B. Onat, E. D. Cubuk, B. D. Malone, and E. Kaxiras, Phys. Rev. B **97**, 094106 (2018).

[37] V. L. Deringer, N. Bernstein, A. P. Bartók, M. J. Cliffe, R. N. Kerber, L. E. Marbella, C. P. Grey, S. R. Elliott, and G. Csányi, J. Phys. Chem. Lett. **9**, 2879 (2018).

[38] N. Bernstein, B. Bhattarai, G. Csányi, D. A. Drabold, S. R. Elliott, and V. L. Deringer, (2018), arXiv:1811.11069 [cond-mat].

[39] H. Jónsson, G. Mills, and K. W. Jacobsen, "Classical and quantum dynamics in condensed phase simulations," (World Scientific, 1998) Chap. Nudged Elastic Band Method for Finding Minimum Energy Paths of Transitions, pp. 385–404.

[40] G. Henkelman, B. Uberuaga, and H. Jónsson, J. Chem. Phys. **113**, 9901 (2000).

[41] V. Lacivita, N. Artrith, and G. Ceder, Chem. Mater. **30**, 7077 (2018).

[42] J. Rohrer and K. Albe, J. Phys. Chem. C **117**, 18796 (2013).

[43] R. Ruffo, S. S. Hong, C. K. Chan, R. A. Huggins, and Y. Cui, J. Phys. Chem. C **113**, 11390 (2009).

[44] E. Hüger, L. Dörrer, J. Rahn, T. Panzner, J. Stahn, G. Lilienkamp, and H. Schmidt, Nano Lett. **13**, 1237 (2013).

[45] J. Li, N. J. Dudney, X. Xiao, Y.-T. Cheng, C. Liang, and M. W. Verbrugge, Adv. Energy Mater. **5**, 1401627 (2014).

[46] W. D. Richards, T. Tsujimura, L. J. Miara, Y. Wang, J. C. Kim, S. P. Ong, I. Uechi, N. Suzuki, and G. Ceder, Nat. Commun. **7**, 11009 (2016).

[47] A. Van der Ven, H.-C. Yu, G. Ceder, and K. Thornton, Prog. Mater. Sci. **55**, 61 (2010).

[48] A. Van der Ven, J. Bhattacharya, and A. A. Belak, Acc. Chem. Res. **46**, 1216 (2013).

[49] M. L. Terranova, S. Orlanducci, E. Tamburri, V. Guglielmotti, and M. Rossi, J. Power Sources **246**, 167.

[50] J. Song, S. Chen, M. Zhou, T. Xu, D. Lv, M. L.Gordin, T. Long, M. Melnyk, and D. Wang, J. Mater. Chem. A **2**, 1257.

[51] Z. Li, A. M. Samuel, F. H. Samuel, C. Ravindran, and S. Valtierra, J. Mater. Sci. **38**, 1203.

[52] A. Jain, S. P. Ong, G. Hautier, W. Chen, W. D. Richards, S. Dacek, S. Cholia, D. Gunter, D. Skinner, G. Ceder, and K. A. Persson, APL Materials **1**, 011002 (2013).

[53] L. Wu, J. Yang, X. Zhou, J. Tang, Y. Ren, and Y. Nie, ACS Appl. Mater. Inter. **8**, 16862 (2016).

[54] H. Sakaguchi, T. Iida, M. Itoh, N. Shibamura, and T. Hirono, IOP Conf. Ser.: Mater. Sci. Eng. **1**, 012030 (2009).

[55] H. Usui, M. Shimizu, and H. Sakaguchi, J. Power Sources **235**, 29 (2013).

[56] H. Usui, M. Nomura, H. Nishino, M. Kusatsu, T. Murota, and H. Sakaguchi, Mater. Lett. **130**, 61 (2014).

[57] J. Perdew, K. Burke, and M. Ernzerhof, Phys. Rev. Lett. **77**, 3865 (1996).

[58] J. P. Perdew, K. Burke, and M. Ernzerhof, Phys. Rev. Lett. **78**, 1396 (1997).

[59] P. E. Blöchl, Phys. Rev. B **50**, 17953 (1994).

[60] G. Kresse and J. Furthmüller, Comput. Mater. Sci. **6**, 15 (1996).

[61] G. Kresse and J. Furthmüller, Phys. Rev. B **54**, 11169 (1996).

[62] R. Byrd, P. Lu, J. Nocedal, and C. Zhu, SIAM J. Sci. Comput. **16**, 1190 (1995).

[63] C. Zhu, R. H. Byrd, P. Lu, and J. Nocedal, ACM T. Math Software **23**, 550 (1997).

[64] J. W. Ponder and F. M. Richards, J. Comput. Chem. **8**, 1016 (1987).

[65] G. Bussi, D. Donadio, and M. Parrinello, J. Chem. Phys. **126**, 014101 (2007).

[66] S. P. Ong, W. D. Richards, A. Jain, G. Hautier, M. Kocher, S. Cholia, D. Gunter, V. L. Chevrier, K. A. Persson, and G. Ceder, Comput. Mater. Sci. **68**, 314 (2013).

[67] A. Urban, D.-H. Seo, and G. Ceder, npj Comput. Mater. **2**, 16002 (2016).

[68] Y. Kubota, M. C. S. E. o, H. Nakanishi, and H. Kasai, J. Appl. Phys. **102**, 053704 (2007).

[69] G. Bergerhoff, R. Hundt, R. Sievers, and I. Brown, J. Chem. Inf. Comput. Sci. **23**, 66 (1983).

[70] B. Key, M. Morcrette, J.-M. Tarascon, and C. P. Grey, J. Am. Chem. Soc. **133**, 503 (2011).

Appendix A: Methods

1. DFT calculations

The baseline method for our simulations is accurate electronic DFT using the Perdew-Burke-Ernzerhof [57, 58] exchange-correlation functional and projector-augmented wave pseudopotentials [59], as implemented in the Vienna Ab-Initio Simulation Package [60, 61]. We employed a plane-wave basis set with an energy cutoff of 520 eV for the representation of the wavefunctions and a gamma-centered k-point grid with a density of 1000 divided by the number of atoms for the Brillouin zone integration. The atomic positions and lattice parameters of all structures were optimized until residual forces were below 20 meV/Å.

2. Artificial neural network potential

The atomic energy network package (ænet) [33] was used for the construction and application of the artificial neural network (ANN) machine-learning potential. ANN potentials are trained to predict the atomic energy based on the local atomic environment [32] from which the atomic forces can be evaluated by analytical differentiation. In this work, the local atomic environment was described by an orthogonal Chebyshev basis [34]. The potential is based on ANNs with two hidden layers and each 15 nodes, using hyperbolic tangent activation functions. For the ANN training, we employed the limited-memory Broyden-Fletcher-Goldfarb-Shanno method [62, 63].

3. Molecular dynamics simulations

All MD simulations were carried out using the Tinker software [64] and the ANN potential via an interface with the ænet package [33]. A time-step of 2 fs was used for the integration of the equation of motion with the Verlet algorithm, and the canonical (NVT) statistical ensemble was imposed with a Bussi-Parrinello thermostat [65].

4. Delithiation protocol

Amorphous *bulk* Li_xSi structures were generated by delithiation of a supercell of the $Li_{15}Si_4$ structure with composition $Li_{480}Si_{128}$. A genetic algorithm coupled with the ANN potential was employed to determine near-ground-state Li-vacancy orderings at each intermediate Li_xSi composition. A schematic of the procedure is shown in Supplementary **Fig. S12**. For the *nanoparticle* delithiation, the initial particle was sequentially delithiated by removing at each step those N Li atoms furthest away from the particle center followed by a thermal equilibration by MD simulation over 1 ns at 500 K, where N was chosen depending on the Li concentration at the particle surface. The Li removal was followed by another MD equilibration over 3 ns at 500 K (i.e., reaching a total of 4 ns). In general, $N = 1000$ Li atoms were removed during each delithiation step. A schematic of the delithiation protocol is shown in Supplementary **Fig. S13**. A slightly elevated temperature was chosen to allow for sufficient redistribution of the Li atoms during the equilibration period, as the simulated delithiation rate is high compared to experimentally realizable currents. As seen in Supplementary **Fig. S8**, the potential energy during the MD simulations converges within 2 ns, so that a total equilibration period of 4 ns is generous.

5. Lithium diffusivity in LiSi bulk structures from MD simulations

For the diffusivity calculations, 5 ns long MD simulations of the bulk $Li_{480-x}Si_{128}$ structures (see above) at temperatures between 400 K and 1200 K were carried out. It was found that all bulk structures generally reached thermal equilibrium after no more than 200 ps, even compositions for which Si segregated during the simulation. To achieve sufficient statistical confidence, the diffusivity was evaluated for 18 MD trajectory parts over each 450 ps after a 200 ps equilibration phase that was discarded. Lithium diffusivities D were obtained by

fitting the Einstein relation

$$6\,D\,t = \left\langle \frac{1}{N} \left|\left| \sum_{i=1}^{N} \Delta\mathbf{r}_i(t) \right|\right|^2 \right\rangle \tag{A1}$$

where t is the time, N is the number of Li atoms in the structure, and $\Delta\mathbf{r}_i$ is the displacement of atom i from its position at $t = 0$. The fits were performed using tools implemented in the pymatgen software package [66]. Using the net displacement instead of the atomic displacement in equation (A1) accounts for correlated motion of Li ions [67]. Only those MD trajectories with a final net displacement larger than 10 Å^2 were analyzed to guarantee sufficient Li hopping. The activation energies for Li diffusion and the diffusivities at room temperature were obtained from Arrhenius fits for temperatures in the range 400–1200 K (Supplementary **Fig. S14**).

Appendix B: Supplementary Information

1. Validation of the Artificial Neural Network Potential

To ensure that the artificial neural network (ANN) potential is reliable for molecular dynamics (MD) simulations of amorphous Li_xSi structures with different compositions, we extensively benchmarked the potential on relevant structures that were not used for the potential training.

Figure S1 shows the distribution of errors in energies predicted by the ANN potential relative to their DFT references for all structures in the test set. As seen in the figure, the error distribution is symmetric and zero-centered, indicating that the space of the reference structures is homogeneously sampled.

Since the main objective of the present work is to understand Li transport in amorphous LiSi, we assessed the reliability of the ANN potential for Li diffusion. A standard technique for the calculation of diffusion barriers in solids is the nudged-elastic-band (NEB) method [39, 40].

Figure S4 shows a comparison of the ANN potential and DFT energies along the minimum energy diffusion paths for two different Li_xSi compositions. The initial and final points of the diffusion path were created by removing neighboring Li atoms from the corresponding Li_xSi structures. Neither the endpoints nor the intermediate structures were included in the ANN potential training. As seen in the figure, the barriers predicted by the ANN potential agree excellently with the DFT results.

NEB calculations require the optimized endpoints of the diffusion as input. In fully amorphous Li_xSi structures, such as in the $Li_{1.00}Si$ phase, the removal of a single Li atom results in significant structural rearrangement which makes NEB calculations challenging.

To obtain a benchmark for Li diffusion in such amorphous structures, we evaluated the energy along interpolated paths in four additional structures with different compositions. In each case, the final structure from a 2 ns long MD trajectory at 600 K was analyzed. The resulting diffusion paths are not minimum energy paths and are rather high in energy, but the comparison of the ANN potential results with the DFT energies allows assessing the reliability of the potential for non-equilibrium structures.

As seen in Figure S5, the agreement between the ANN potential energies and DFT is very good despite the high-energy structures along the interpolated paths. Only for the

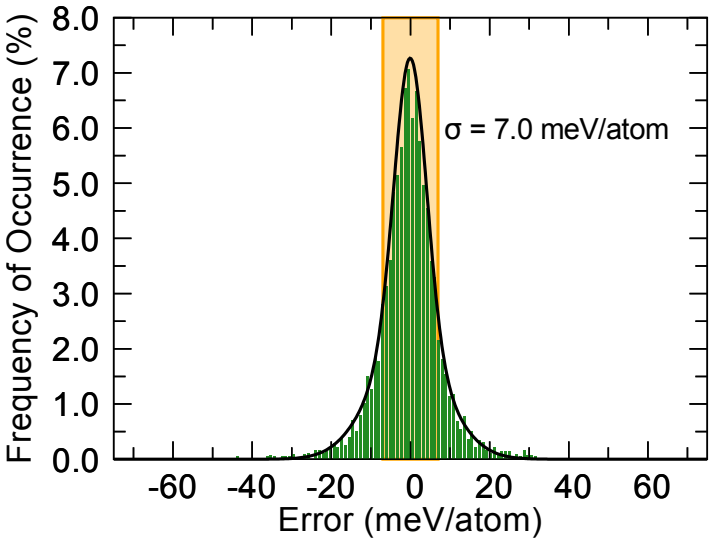

FIG. S1. **Error distribution in the test set used for the validation of the ANN potential.** The test set comprises 4,516 structures that were randomly selected from the reference data set and were not used for the training of the ANN potential. The orange region indicates the standard deviation of ∼7.0 meV/atom of the fitted distribution (black lines). The root mean squared error (RMSE) of the ANN potential energy is ∼7.7 meV/atom, which includes the tails that are not captured by the fitted distribution (the sum of two normal distributions). The RMSE of the training set is ∼6.3 meV/atom.

$Li_{3.75}Si$ composition the ANN potential deviates significantly from DFT for structures that are more than 2 eV above the minimum. However, even for the $Li_{3.75}Si$ composition, the ANN potential reproduces the minimum energy path well, as shown in Figure S4.

Finally, we assessed the reliability of the ANN potential for actual MD simulations by comparing the energies of structures during the initial and final 50 ps of MD trajectories at $T = 1000$ K. As seen in Figure S6, the agreement between the ANN potential and DFT is remarkable. Deviations increase with decreasing Li content but never exceed 10 meV/atom. An even closer agreement can be expected for lower temperatures that give rise to less distorted structures during the MD simulation. This comparison also confirms that the MD simulations with the ANN potential do not result in trapping in artificially stabilized phases.

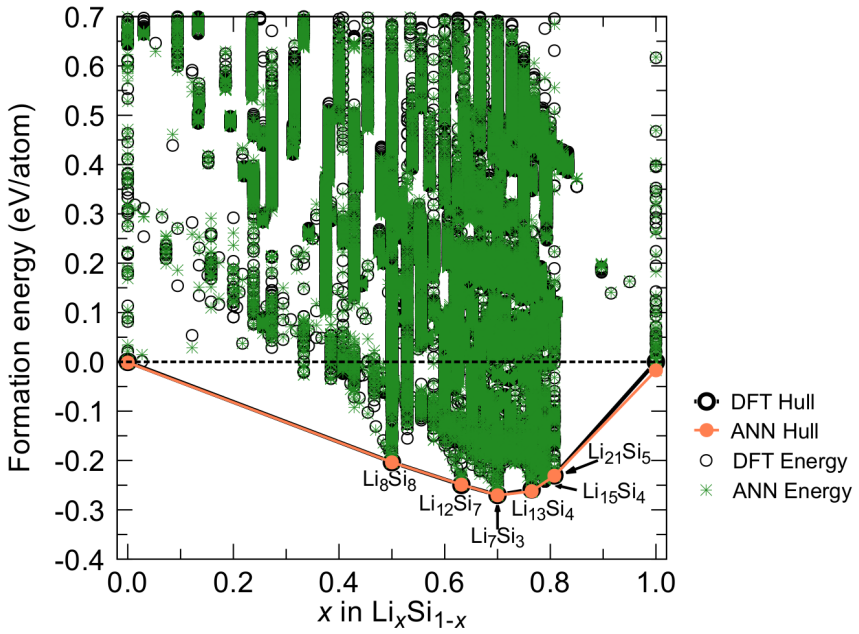

FIG. S2. Comparison of the formation energies of Li_xSi_{1-x} structures as predicted by the artificial neural network (ANN) potential (green stars) with their density-functional theory (DFT) reference energies (black circles). The black and yellow lines and filled circles indicate the lower convex hulls of the DFT and ANN energies, respectively. The ANN potential ground states are in excellent agreement with DFT. Note that this plot shows the formation energies of structures from the entire reference data set.

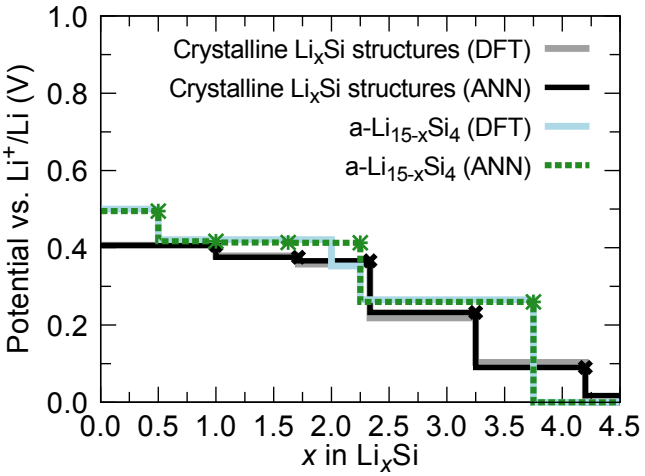

FIG. S3. Comparison of computational 0 K voltage profiles of the thermodynamic ground state phases of the LiSi alloy and of amorphous a-$Li_{15-x}Si_4$ phases predicted by DFT and the ANN potential. As seen in the figure, the voltage profile predicted by the ANN potential is nearly identical to the DFT voltage profile, further confirming the accuracy of the potential. Note that the crystalline Li_xSi structures were included in the ANN potential training set.

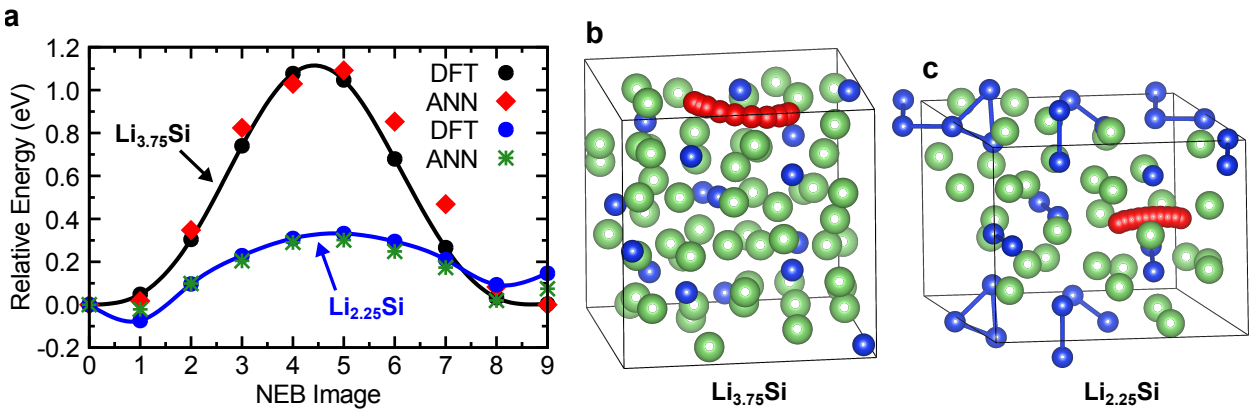

FIG. S4. **Comparison of the ANN potential and DFT activation energies for Li diffusion in two Li_xSi structures with different composition.** **a**, Energy along the minimum energy pathways for Li diffusion in $Li_{3.75}Si$ and $Li_{2.25}Si$ as calculated using the nudged elastic band method (NEB). Black and blue circles indicate the DFT energies for the NEB images, red diamonds and green stars are the corresponding ANN potential energies. The lines are cubic splines to guide the eye. **b** and **c**, Selected Li diffusion pathway in the $Li_{3.75}Si$ (= $Li_{60}Si_{16}$) structure and in the $Li_{2.25}Si$ ($Li_{36}Si_{16}$) structure, respectively. Si atoms are colored blue, Li green, and the NEB images red. Neither the endpoints nor the NEB images were included in the ANN potential training set.

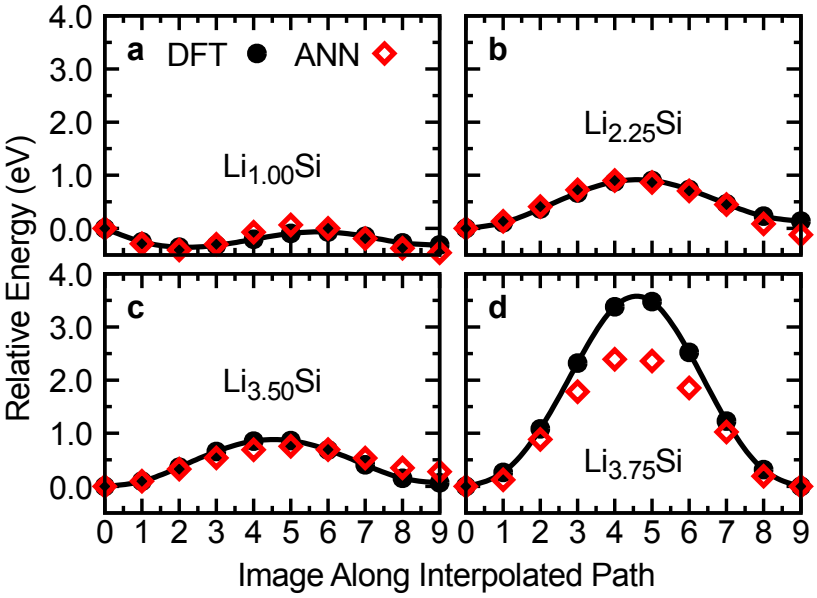

FIG. S5. **Energy along interpolated paths in Li_xSi structures with four different compositions.** In contrast to the NEB paths shown in Figure S4, the paths shown in this figure are not minimum energy diffusion paths. The DFT energies are shown as black circles; the corresponding ANN potential energies as red diamonds.

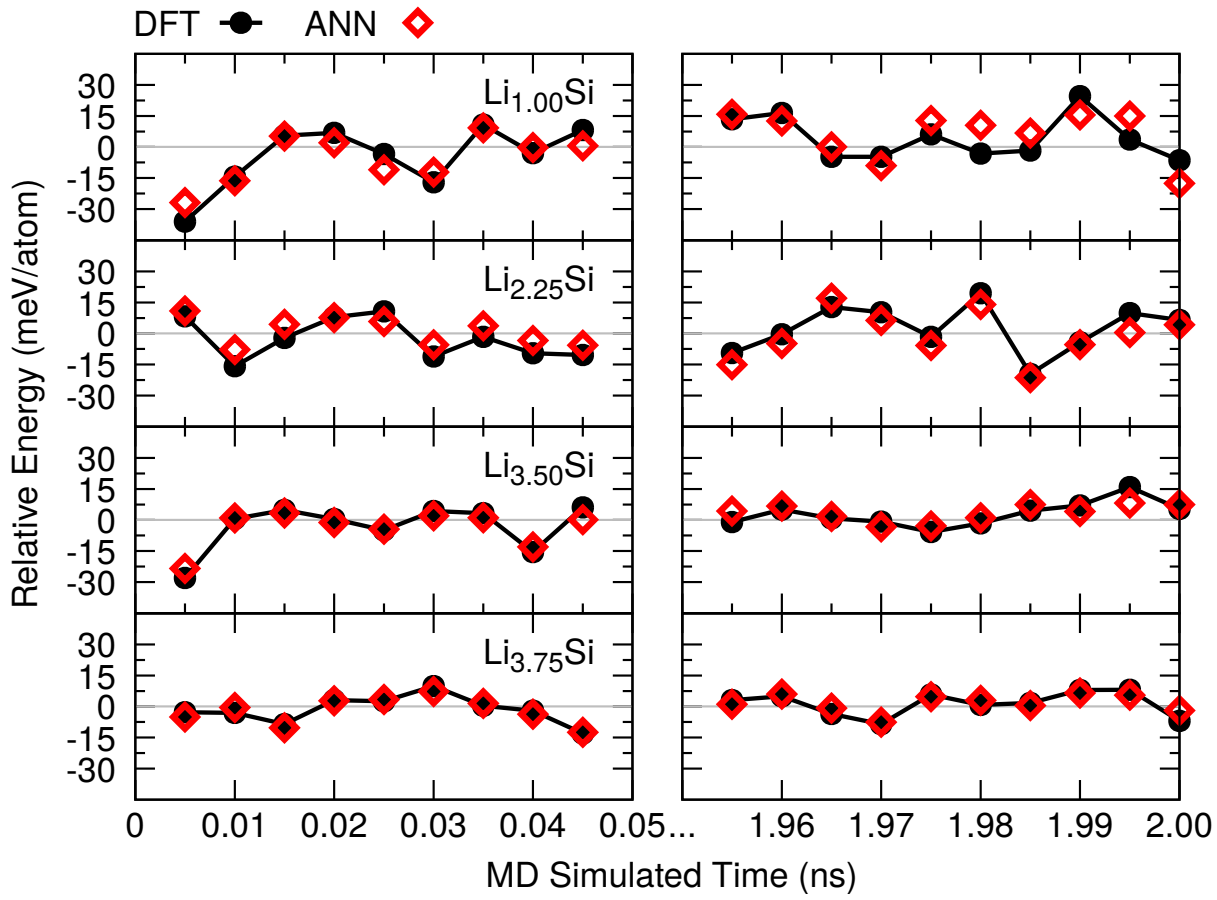

FIG. S6. **Comparison of energies along MD trajectories: bulk $Li_{15}Si_4$ (Li = 480, 448, 288, and 128 atoms).** Energies during the initial (left) and final (right) 50 ps of 2 ns long MD trajectories are shown. The ANN potential energies are shown as red diamonds, and the corresponding DFT energies are black circles.

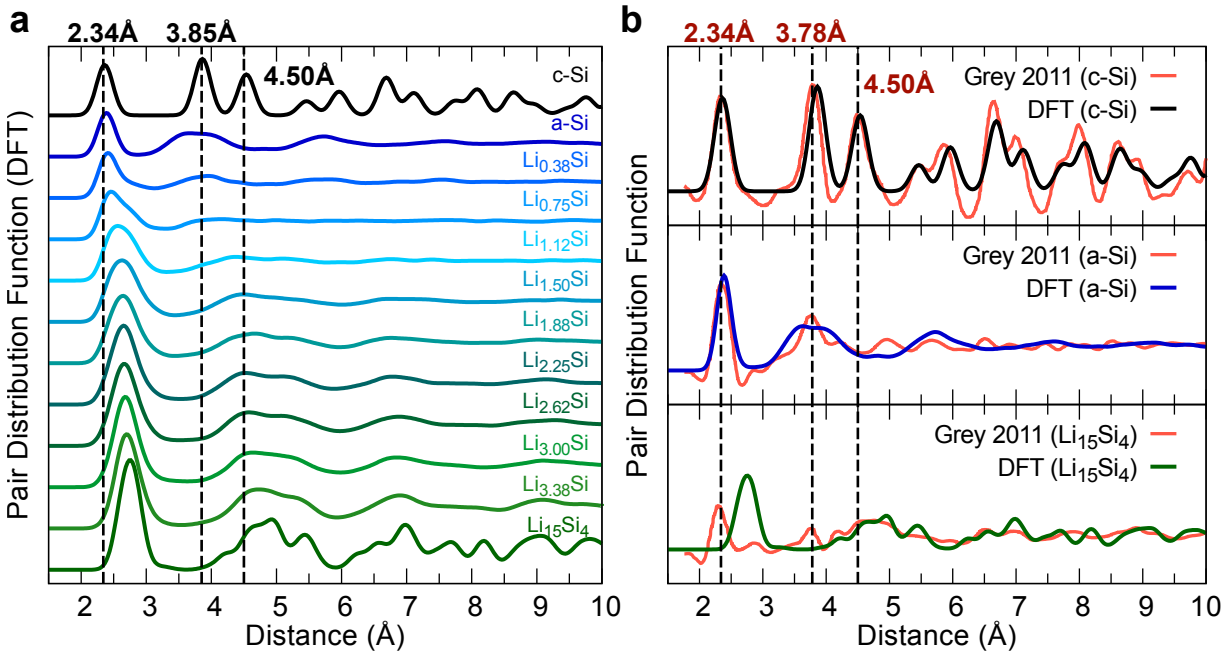

FIG. S7. **Pair distribution functions for crystalline and amorphous LiSi.** **a**, Calculated pair distribution functions (PDFs) of crystalline silicon (black) and c-$Li_{15}Si_4$ (green) and amorphous a-$Li_{15-x}Si_4$ structures with intermediate compositions (shades of blue). The PDFs of the a-$Li_{15-x}Si_4$ compositions were obtained from DFT optimized structures based on the $Li_{480}Si_{128}$ composition. At each composition, the lowest energy atomic configuration among the corresponding $Li_{480-x}Si_{128}$ structures with DFT-optimized geometry and cell parameters was considered. The $Li_{15}Si_4$ crystal structure was taken from the international crystal structure database (ICSD ID: 159397) and optimized with DFT for consistency [68, 69]. The atomic scattering factors were approximated by the atomic mass. All PDFs were convoluted with Gaussian functions with a full width at half maximum (FWHM) of 0.3 Å to simulate experimental resolution. **b**, Comparison of the computed PDFs for c-Si, a-Si, and c-$Li_{15}Si_4$ with measurements from reference 70. Both, the predicted intensities and peak positions of the computed PDF for crystalline silicon are in excellent agreement with the measured reference (top panel), indicating that the DFT lattice parameters are close to the real values. The measured PDFs for the $Li_{15}Si_4$ structure (bottom panel) contains a number of intensities that are not present in the computed PDF. Most notably, the first and second neighbor peaks of c-Si are present in the X-ray $Li_{15}Si_4$ PDF showing that unlithiated silicon was still present in the measured sample. Similarly, all computed intensities of the amorphous silicon structure obtained from complete delithiation of the $Li_{480}Si_{128}$ structure are present in the measured PDF, but the measured PDF contains additional correlations that can be attributed either to remaining c-Si or to residual lithium in the material (peaks at 5.0 Å and 6.5 Å).

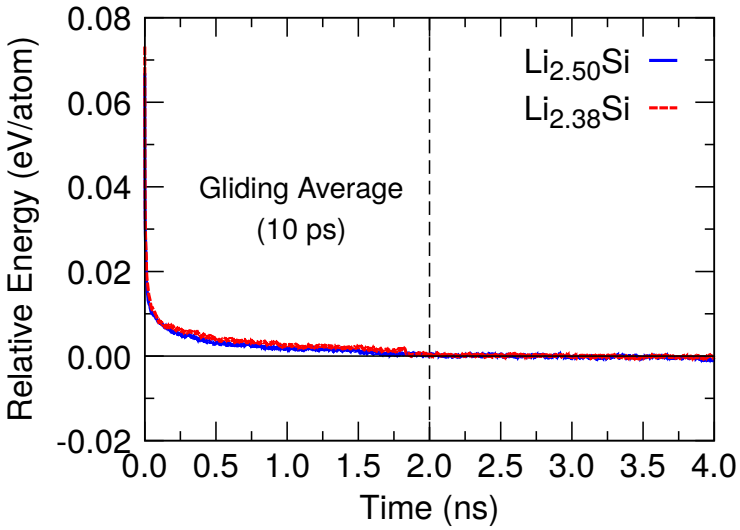

FIG. S8. **The nanoparticle structure have reached thermal equilibrium after 2 ns long molecular dynamics simulations at 500 K.** Gliding average (10 ps) of the potential energy during molecular dynamics simulation of two nanoparticle models with compositions $Li_{6429}Si_{2571}$ (= $Li_{2.50}Si$, blue line) and $Li_{6336}Si_{2664}$ (= $Li_{2.38}Si$, red dashed line) at 500 K. After around 2 ns the potential energy is within 2 meV/atom of the final structure, indicating that the system has reached thermal equilibrium.

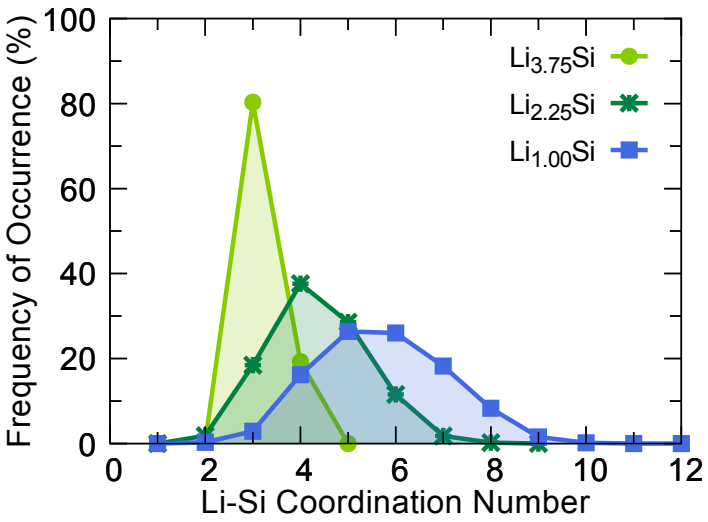

FIG. S9. **On average Li is coordinated by more Si atoms at more delithiated compositions but the probability of low coordinated Li atoms also increases.** Number of Si atoms within a range of 3.5 Å from each Li atom during molecular dynamics simulations at 600 K over 5 ns. In the crystalline $Li_{3.75}Si$ (= $Li_{15}Si_4$) structure, a Li atom is coordinated either by 3 or 4 Si atoms with around 99% probability.

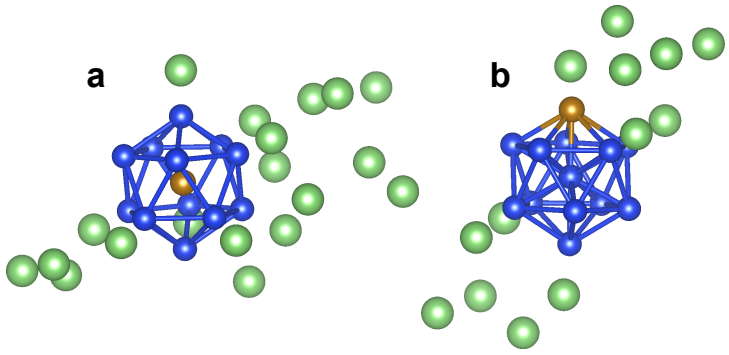

FIG. S10. **Initial ideal icosahedral structures of the doped cluster models.** Initial structure of the **a**, *core*-doped and **b**, *shell*-doped cluster models used to estimate the potential for Si clustering. Dopants that favor core-doping over shell-doping and bind strongly with Si are expected to promote Si clustering. Li atoms are colored green, Si is blue, and the dopant is brown.

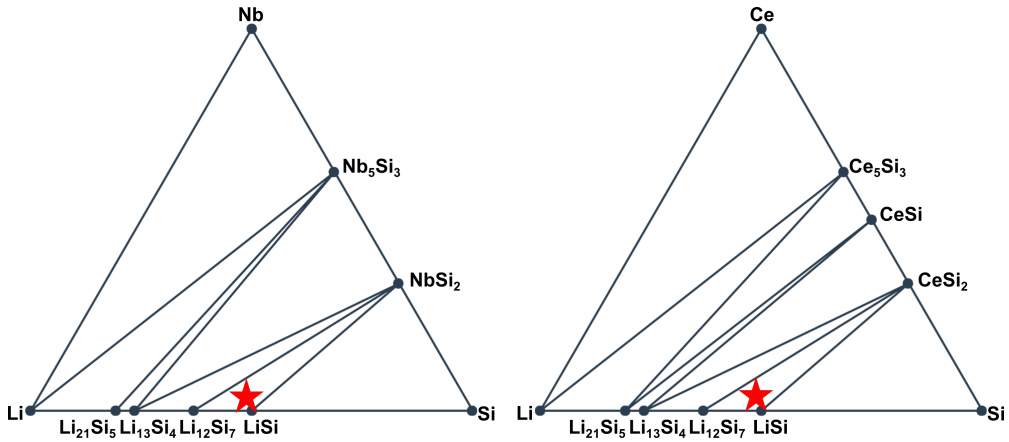

FIG. S11. **Ab initio phase diagrams of Nb and Ce compounds with Li and Si.** The phase diagrams were generated based on the ab initio calculations of inorganic materials provided by the *Material Project* database [52]. For both Nb and Ce compounds with Si are database but no compounds with Li. The red star indicates the $Li_{13}Si_{12}X$ compositions of the investigated doped cluster models (Figure S10).

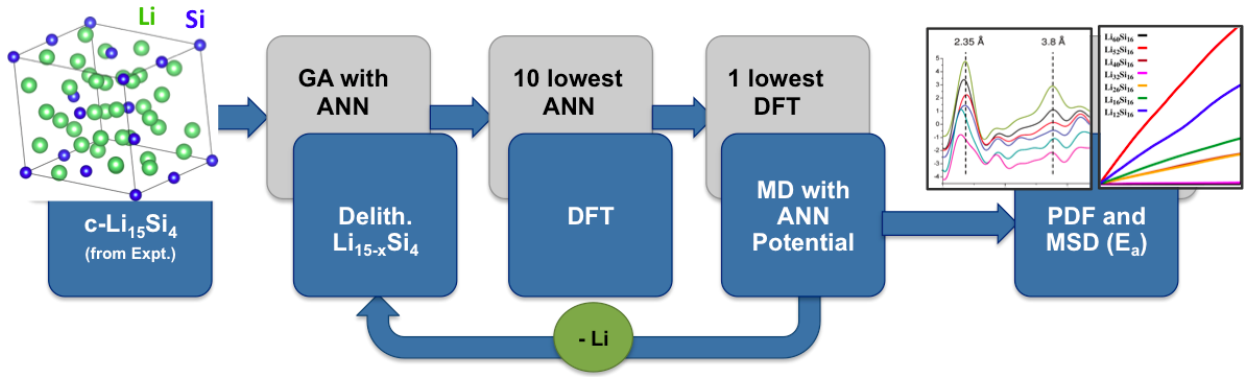

FIG. S12. Schematic of the structure-determination protocol used for the sampling of bulk $Li_{15-x}Si_4$ structures. Different supercells of the experimental c-$Li_{15}Si_4$ structure with compositions up to $Li_{480}Si_{128}$ were used as starting points. From these structures, Li atoms were sequentially removed, and at each delithiated composition the lithium-vacancy ordering was determined with a genetic algorithm (GA). The geometry and cell parameters of the 10 lowest-energy configurations were subsequently optimized with DFT. The most stable structures at each composition were used as input for MD simulations.

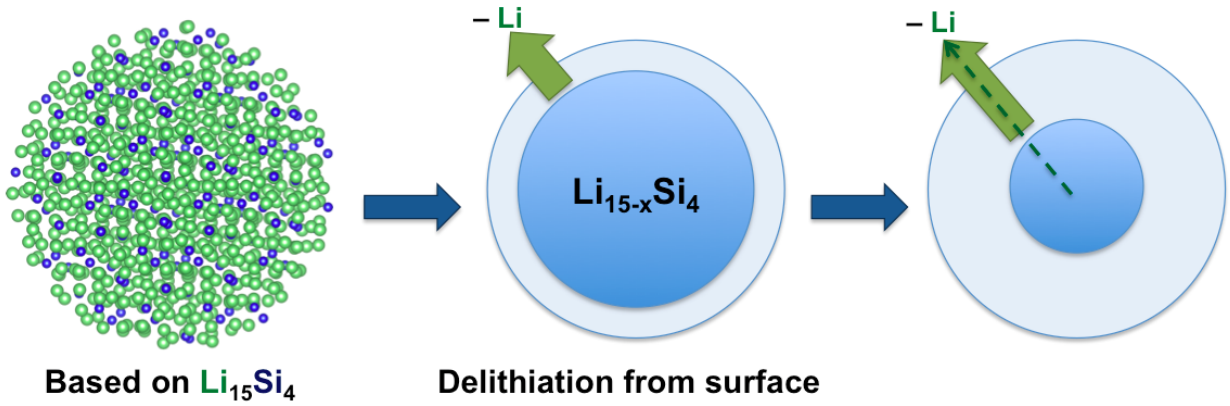

FIG. S13. Schematic of the protocol used for the delithiation of LiSi nanoparticles. At each step, Li atoms were removed from the surface of the particle, followed by a molecular dynamics simulation at 500 K over 4 ns.

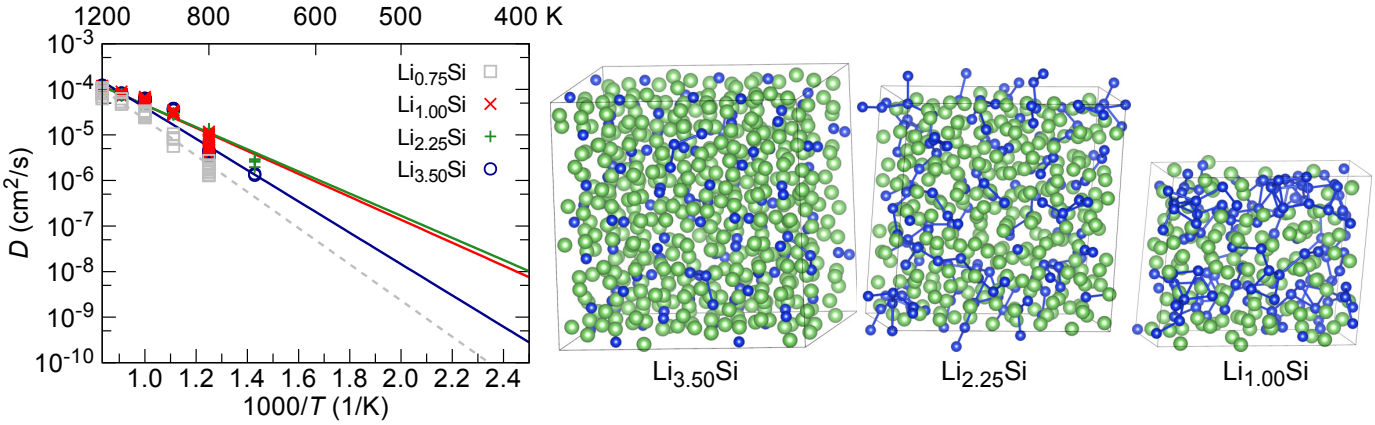

FIG. S14. **Arrhenius extrapolation of the Li diffusivities in $Li_{3.75-x}Si$ structures to room temperature.** The data is based on 5 ns long molecular dynamics simulations of structures containing 128 Si atoms and between 96 and 480 Li atoms ($Li_{480-x}Si_{128}$). Only molecular dynamics trajectories with Li mean squared displacement greater than 10 Å^2 were considered. The corresponding room temperature diffusivities and activation energies are given in Table 1 in the main manuscript. For the sake of completeness, here the composition $Li_{0.75}Si$ is also included to show that the diffusivity decreases once the Li content drops below $Li_{1.00}Si$. Also shown are the structures of $Li_{448}Si_{128}$ (= $Li_{3.50}Si$), $Li_{288}Si_{128}$ (= $Li_{2.25}Si$), and $Li_{128}Si_{128}$ (= $Li_{1.00}Si$) after 2 ns MD equilibration at $T = 600$ K.

2. Supplementary Tables

TABLE S1. Measured room-temperature Li diffusivity as reported in the literature. Experimentally, the Li diffusivity has been obtained from electrochemical impedance spectroscopy (EIS), cyclic voltammetry (CV), galvanostatic intermittent titration (GITT), and by potentiostatic intermittent titration (PITT).

D **(cm^2/s)**	**Method**	**Reference**
10^{-10}	EIS	[43]
10^{-12}	CV, EIS, GITT	[6]
10^{-14}	EIS, PITT	[7]
10^{-14}–10^{-13}	PITT	[8]